Sensitivity Analysis of Broadband Shock-Associated Noise based on Navier-Stokes Equations Decomposition

Trushant K. Patel* and Steven A. E. Miller†
University of Florida, Gainesville, FL 32611

Broadband shock-associated noise (BBSAN) is generated due to the coherent interaction of the large-scale turbulent eddies with the shock-cell structure. The source term responsible for BBSAN is identified from the Navier-Stokes equations, and consists of the dot product of the gradient of mean pressure and the fluctuating velocities. A closed form model is developed for the prediction of BBSAN using the identified source term. This model is used to investigate the sensitivity of BBSAN. A method of characteristics nozzle and a biconic nozzle are used for the sensitivity analyses. A sensitivity analysis is performed for the source term and peak noise is predicted, where the dependent arguments are the nozzle pressure ratio, the total temperature ratio, and the area ratio. The effect of input conditions on the variation in the axial source location is studied. We also examine the influence of exit boundary layer profiles and turbulence on the BBSAN using both the nozzles. The biconic nozzles are observed to be less sensitive relative to the method of characteristics nozzle for all the parameters investigated.

Nomenclature

Symbols	Description
c_p	specific heat at constant pressure
c_v	specific heat at constant volume
$c_l, c_\perp, c_\tau, c_u$	constants
c_∞	ambient speed of sound
D	diameter of nozzle
D_j	fully-expanded jet diameter
E_u	energy spectrum for velocity
e	internal energy
K	turbulent kinetic energy
L	shock-cell spacing
l	turbulent length scale in streamwise direction
$l_\perp$	turbulent length scale in cross-stream direction
p	pressure
p_∞	ambient pressure
q	field-variable
$\overline{q}$	time averaged base flow
$\hat{q}$	anisotropic fluctuations
$\check{q}$	isotropic fluctuations
q'	radiation due to anisotropic fluctuation
q''	radiation due to isotropic fluctuation
$\underline{q}$	summation of base and aerodynamic fluctuations
$\overline{q}^\perp$	summation of acoustic fluctuations
q_g	vector Green's function
$\tilde{q}$	Fourier transform of q
q^*	complex conjugate of q
$R_{m,n}$	two-point space-time cross-correlation of source terms
$\mathcal{R}$	universal gas constant
r	distance between source and observer locations
S_k	k$^{\text{th}}$ spectral density
T	temperature
t	time
$\boldsymbol{u}$	velocity vector
u_c	eddy convection velocity
$\boldsymbol{x}$	spatial position
$\mathbf{x}$	observer location
$\mathbf{y}$	source location

Greek Symbols	
β	off-design parameter
γ	ratio of specific heats
δ_{ij}	Kronecker delta function
δ	Dirac delta function
ϵ	turbulent dissipation rate
$\boldsymbol{\eta}$	source separation vector
Θ_n	source terms
θ	polar observer angle
κ	wavenumber
λ	thermal conductivity
μ	dynamic viscosity
ρ	density
ρ_∞	ambient density
τ	source emission time
τ_s	turbulent time scale
$\Delta\tau$	time delay between sources
Ω	specific dissipation rate
ω	angular frequency

Non-Dimensional Numbers	
M_c	convective Mach number
M_d	design Mach number
M_j	fully-expanded jet Mach number
Pr	Prandtl number
St	Strouhal number

Abbreviations	
BBSAN	broadband shock-associated noise
FUN3D	fully unstructured Navier-Stokes
LEE	linearized Euler equations
LES	large-eddy simulation
MOC	method of characteristics
NPR	nozzle pressure ratio
OASPL	overall sound pressure level
RANS	Reynolds-averaged Navier-Stokes
SHJAR	small hot jet acoustic rig
SPL	sound pressure level
TTR	total temperature ratio

*Graduate Research Assistant, Department of Mechanical and Aerospace Engineering, University of Florida, P.O. Box 116250, Gainesville, FL, 32611, USA, trushant@ufl.edu, and AIAA Student Member

†Assistant Professor, Department of Mechanical and Aerospace Engineering, University of Florida, P.O. Box 116250, Gainesville, FL, 32611, USA, saem@ufl.edu, and AIAA Lifetime / Senior Member

I. Introduction

Jet noise is one of the loudest sounds generated by humans. The intensity of jet noise on an aircraft carrier deck ranges from 120 to 150 dB at peak frequencies [1]. The noise is detrimental to the health and hearing of the military personnel working in close proximity to the aircraft on an aircraft carrier. Approximately 800 million dollars were spent by the US Department of Veterans Affairs for hearing loss disability benefits in 2005. That number has risen to over a billion dollars in the current decade [1]. Oblique shocks and expansions are generated within the jet exhaust when the pressure at the exit of the nozzle is different than the atmospheric pressure. This is often observed during take-off when the engine of the jet is operated at an under-expanded condition to maximize the thrust. These shocks interact with the large-scale turbulent structures in the shear layer and generate shock-associated noise.

In addition to turbulent mixing noise, shock-associated noise is a component of jet noise observed in off-design supersonic jets. Shock-associated noise consists of two main components, broadband shock-associated noise (BBSAN) and 'screech' tones. Screech tones primarily radiate in the upstream direction towards the nozzle and occurs at multiple discrete frequencies. Screech tones are easily eliminated by modifying the nozzle lip profile, and are generally not present on full-scale engines. However, BBSAN is generated because of the coherent interaction of large-scale turbulent structures with the shock-cell structure and is broadband in nature. In this paper, we perform sensitivity analyses of BBSAN using a closed-form model developed using an acoustic analogy based on the Navier-Stokes equations.

Various prediction models based on the physical mechanism of BBSAN have been proposed by different investigators. Harper-Bourne and Fisher [2] were the first to investigate and develop an empirical model of the two-point cross-correlation of pressure at different shock locations to predict BBSAN. They argued that the large-scale turbulent structures interact with multiple shocks in the jet exhaust and emit acoustic radiation. Harper-Bourne and Fisher [2] also observed that the BBSAN scales as β^4, where β is the off-design parameter. Overcoming some of the limitations of the Harper-Bourne and Fisher [2] model, a theory based on the physics of BBSAN was proposed by Tam and Tanna [3]. Later, Tam [4] developed a stochastic model that built upon the theory of Tam and Tanna [3]. Tam [4] super-imposed the instability wave model of Tam and Chen [5] with different wave-guide modes of the shock-cell structure following the work of Pack [6]. The interaction between the instability wave and different wave-guide modes generated different spectral peaks of BBSAN. Tam [4] used the method of matched asymptotic expansions to solve for the pressure in the near- and far-field. The amplitude of pressure was approximated by an analytical model, and the spectral density of pressure was found using the Fourier transform of the auto-correlation of pressure.

Using the work of Tam [4] as a basis, Morris and Miller [7] developed an acoustic analogy based model using linearized Euler equations (LEE) for predicting the BBSAN. They used Reynolds-averaged Navier-Stokes (RANS) computational fluid dynamics (CFD) simulations as an argument to their model. As a result, their model was able to predict BBSAN for a wide range of jet operating conditions as well as for different nozzle geometries. They performed the convolution integral of the two-point space-time cross-correlation of the source term with the vector Green's function to develop a model for predicting the spectral density of pressure. The source term was obtained using scaling analysis of the unsteady force per unit volume associated with the turbulent velocity fluctuations and velocity perturbations associated with the shock-cells. Suzuki [8] created a model to predict BBSAN using wave-packets and large-eddy simulation (LES). He created a semi-empirical model of the cross-correlation of the proper orthogonal decomposition modes of the near-field LES data, and used those to predict the sound pressure level (SPL) at different Strouhal numbers in the far-field. In the present work, we develop a model using the identified source term of BBSAN. Based on the identified source term and the developed model, we study the effect of nozzle pressure ratio (NPR), total temperature ratio (TTR), and area ratio on the radiated noise.

Extensive experiments were performed by Tanna [9], Seiner and Norum [10, 11], Norum and Seiner [12–14], and Seiner and Yu [15] to understand the dependence of BBSAN on various input parameters. Seiner and Norum [10] compared the reduction of shock-associated noise from an under-expanded convergent nozzle with different convergent-divergent nozzles for the same thrust. Norum and Seiner [12], and Tanna [9] observed that the BBSAN becomes important relative to the turbulent mixing noise when the NPR deviates from the design condition, TTR decreases, and when the observer is not in the downstream radiation direction. Different experiments were performed by Bridges and Wernet [16], Viswanathan et al. [17], and Kuo et al. [18] to understand the effect of temperature on BBSAN. A numerical study on the effect of temperature on BBSAN was performed by Miller [19] using the Morris and Miller [7] model. It was observed that the BBSAN increases with increase in TTR to a certain level and remains constant thereafter. Viswanathan et al. [17] observed that the scaling of BBSAN deviates from β^4 at higher TTR. For a given NPR, the intensity of the shock-cell structure in the exhaust of the nozzle can be controlled by controlling the area ratio of the nozzle. Variable area nozzles are used in various military aircrafts such as F-15 and F-16, and were studied by Mabe [20] and Michel [21].

For subsonic jet noise, Zaman [22] compared the noise from two nozzles having different exit boundary layer profiles. He found the nozzle with a laminar boundary layer at the nozzle exit to be noisier than the nozzle with a turbulent boundary layer. Bogey and Bailly [23] and Bogey et al. [24] studied the effect of boundary layer profile at the exit of the nozzle numerically using LES. They tripped the boundary layer inside the nozzle and observed that the jet noise reduces for turbulent boundary layer profiles. Brès et al. [25] related the reduction of noise from the turbulent boundary layer to the difference in growth rate of the Kelvin-Helmholtz modes in the near nozzle region observed for varying boundary layer profiles. As BBSAN is generated due to the coherent interaction of the large-scale turbulent structures with the shock-cell structure, any effect on the large-scale turbulent structure by the boundary layer may affect the BBSAN.

Sensitivity analysis is a method to analyse the effect of different input parameters on the output. Sensitivity analysis have been performed at an aircraft level for different noise generating sources from an aircraft at varying angles and frequencies by Huber and Illa [26]. Sensitivity analysis and shape optimization has been performed by Rumpfkeil and Zingg [27] to reduce the trailing edge noise from an airfoil. Sensitivity analysis can also be used to understand the parameters responsible for jet noise. Controlling the input parameter which has the maximum effect on the radiated noise can help in the reduction of jet noise. Freund [28] and Kim et al. [29] performed sensitivity analysis using adjoint based methods in conjunction with LES to reduce the noise from an ideally expanded Mach 1.3 turbulent jet. A reduction of 3.5 dB was obtained by Kim et al. [29] by controlling the parameters in the near nozzle region of the jet.

In the current work, we quantify the sensitivity of BBSAN with various input parameters such as NPR, TTR, nozzle geometry, and thickness of the exit boundary layer. Identifying the input parameter which is most sensitive for BBSAN, will enable us to design or select the most effective noise reduction technique for BBSAN. Based on the sensitivity analysis, design choices can be made that do not increase the BBSAN. The source term for BBSAN has been identified by Patel and Miller [30] using an acoustic analogy based on the decomposition of the Navier-Stokes equations developed by Miller [31]. A closed-form model for prediction of BBSAN has been created by convolving the two-point cross-correlation of the identified source term with the vector Green's function. This model and the identified source term are used in the current work for sensitivity analysis of BBSAN.

The rest of the paper is organized as follows. The mathematical model based on the decomposition of the Navier-Stokes equations [31] is summarized in Section II.A. The vector Green's function is derived in Section II.B, the source terms for BBSAN are identified in Section II.C, and the implementation of the model is discussed in Section II.D. Sensitivity analyses of the source term with different input parameters is performed in Section III. Finally, the summary and conclusions are discussed in Section IV.

II. Source Term for BBSAN

A. Mathematical Model

The approach of Miller [31] based on the decomposition of the Navier-Stokes equations is described using a flowchart in Fig. 1. The Navier-Stokes equations are used as the governing equations. The field-variables such as pressure, velocity, temperature, and density are decomposed as $q = \overline{q} + \breve{q} + \hat{q} + q' + q''$, where q is any field-variable. The over-bar operator represents time-averaged base flow, breve operator represents spatially incoherent isotropic turbulent fluctuations, while the hat operator indicates large-scale coherent anisotropic turbulent fluctuations. A single and double prime indicates the radiating acoustic fluctuations due to the anisotropic and isotropic turbulence, respectively. The decomposed field-variables are substituted into the governing equations, and the resulting equations are rearranged such that the radiating acoustic quantities are on the left hand side of the equations, while the source terms involving the base flow and aerodynamic turbulent fluctuations are brought to the right hand side. The resultant sources of sound are written as two-point cross-correlations involving each term of the Navier-Stokes equations. The propagators on the left hand side are linearized. The solution to the linearized Navier-Stokes equations in a quiescent environment is obtained using a vector Green's function. The spectral density of acoustic pressure is obtained by convolving the vector Green's function with the two-point cross-correlation of the source term.

Miller [31] used this approach to predict the noise from isotropic turbulence. However, since the acoustic analogy is based on the Navier-Stokes equations, it contains all the noise sources. In the present work, we use the acoustic analogy approach of Miller [31] to identify the BBSAN source term and perform a sensitivity analysis of the BBSAN source. Based on the work of Miller [31], the spectral density of any field-variable is written as

$$S_k^{\perp}(\mathbf{x},\omega) = \int_{-\infty}^{\infty} \dots \int_{-\infty}^{\infty} \sum_{m=0}^{4} \sum_{n=0}^{4} \tilde{q}_g^{*\perp,m}(\mathbf{x};\mathbf{y},\omega) \tilde{q}_g^{\perp,n}(\mathbf{x};\mathbf{y}+\boldsymbol{\eta},\omega) R_{m,n}^{\perp}(\mathbf{y},\boldsymbol{\eta},\tau) \exp\left[i\omega\tau\right] d\tau d\boldsymbol{\eta} d\mathbf{y}, \tag{1}$$

where S_k denotes the spectral density of the k^{th} field-variable, $\mathbf{x}$ and $\mathbf{y}$ denotes the observer and source location, respectively, and ω is the angular frequency. The vector Green's function is written in terms of the field-variable as $q^{\perp n}_{k,g} = [\rho^{\perp n}_g, \boldsymbol{u}^{\perp n}_{i,g}, p^{\perp n}_g]^T$, where ρ, $\boldsymbol{u}$, and p represents density, velocity, and pressure, respectively. The superscript $\perp$ on the field-variables denotes the summation of the radiating fluctuations due to anisotropic and isotropic turbulence respectively, i.e. $q^{\perp} = q' + q''$. The tilde operator $\tilde{q}$ represents the Fourier transform of the field-variable q, the asterisk superscript q^* represents the complex conjugate of the complex variable q, and the subscript g denotes the vector Green's function. The vector Green's function satisfies

$$\frac{\partial \rho^{\perp n}_g}{\partial t} + \frac{\partial}{\partial x_j}\left(\underline{\rho} u^{\perp n}_{j,g} + \rho^{\perp n}_g \underline{u}_j\right) = \delta(\mathbf{x}-\mathbf{y})\delta(t-\tau)\delta_{0n}, \tag{2}$$

$$\begin{aligned}\frac{\partial}{\partial t}\left(\underline{\rho} u^{\perp n}_{i,g} + \rho^{\perp n}_g \underline{u}_i\right) + \frac{\partial}{\partial x_j}\left(\underline{\rho u}_i u^{\perp n}_{j,g} + \underline{\rho} u^{\perp n}_{i,g}\underline{u}_j + \rho^{\perp n}_g \underline{u}_i \underline{u}_j\right) + \frac{\partial p^{\perp n}_g}{\partial x_j}\delta_{ij} \\ - \frac{\partial}{\partial x_j}\left[\mu\left(\frac{\partial u^{\perp n}_{i,g}}{\partial x_j} + \frac{\partial u^{\perp n}_{j,g}}{\partial x_i}\right)\right] + \frac{2}{3}\frac{\partial}{\partial x_j}\left[\mu \frac{\partial u^{\perp n}_{k,g}}{\partial x_k}\right] = \delta(\mathbf{x}-\mathbf{y})\delta(t-\tau)\delta_{in},\end{aligned} \tag{3}$$

and

$$\begin{aligned}&\frac{\partial p^{\perp n}_g}{\partial t} + \frac{\gamma-1}{2}\frac{\partial}{\partial t}\left(\rho^{\perp n}_g \underline{u}_k \underline{u}_k + 2\underline{\rho} u^{\perp n}_{k,g}\underline{u}_k\right) + \frac{\gamma-1}{2}\frac{\partial}{\partial x_j}\left(\rho^{\perp n}_g \underline{u}_j \underline{u}_k \underline{u}_k + \underline{\rho} u^{\perp n}_{j,g}\underline{u}_k\underline{u}_k + 2\underline{\rho u}_j u^{\perp n}_{k,g}\underline{u}_k\right) \\ &+ \gamma\frac{\partial}{\partial x_j}\left(u^{\perp n}_{j,g}\underline{p} + \underline{u}_j p^{\perp n}_g\right) - (\gamma-1)\frac{\partial}{\partial x_j}\left[\frac{c_p\mu}{Pr}\frac{\partial T^{\perp n}_g}{\partial x_j}\right] - (\gamma-1)\frac{\partial}{\partial x_j}\left[\mu u^{\perp n}_{i,g}\left(\frac{\partial \underline{u}_i}{\partial x_j} + \frac{\partial \underline{u}_j}{\partial x_i}\right) + \mu\underline{u}_i\left(\frac{\partial u^{\perp n}_{i,g}}{\partial x_j} + \frac{\partial u^{\perp n}_{j,g}}{\partial x_i}\right)\right] \\ &+ (\gamma-1)\frac{2}{3}\delta_{ij}\frac{\partial}{\partial x_j}\left[\mu u^{\perp n}_{i,g}\frac{\partial \underline{u}_k}{\partial x_k} + \mu\underline{u}_i\frac{\partial u^{\perp n}_{k,g}}{\partial x_k}\right] = \delta(\mathbf{x}-\mathbf{y})\delta(t-\tau)\delta_{4n}.\end{aligned} \tag{4}$$

The under-bar operator in Eqs. (2) to (4) denotes the sum of the base quantity and fluctuating quantities, i.e. $\underline{q} = \overline{q} + \hat{q} + \breve{q}$. The Dirac delta function and the Kronecker delta function are δ and δ_{ij}, respectively. Calorically perfect gas equations such as $p = \rho\mathcal{R}T$, $e = c_v T$, $\mathcal{R} = c_p - c_v$, and $\gamma = c_p c_v^{-1}$ are used for closure, where T is temperature, $\mathcal{R}$ is the universal gas constant, e is the internal energy, and c_p and c_v are the specific heats at constant pressure and volume, respectively. The Prandtl number is denoted by $Pr = c_p\mu\lambda^{-1}$, where μ is the dynamic viscosity and λ is the thermal conductivity. Note that the energy equation is converted to the pressure form using the calorically perfect gas equations, as we are interested in the pressure of the sound field at the observer location. The source emission time and the observer time are denoted by τ and t, respectively.

The two-point space-time cross-correlation of the source terms in Eq. (1) is denoted by $R_{m,n}(\mathbf{y}, \boldsymbol{\eta}, \tau)$ and written as

$$R^{\perp}_{m,n}(\mathbf{y}, \boldsymbol{\eta}, \tau) = \langle \Theta_m(\mathbf{y}, \tau)\Theta_n(\mathbf{y} + \boldsymbol{\eta}, \tau + \Delta\tau)\rangle = \int_{-\infty}^{\infty} \Theta_m(\mathbf{y}, \tau)\Theta_n(\mathbf{y} + \boldsymbol{\eta}, \tau + \Delta\tau) d\Delta\tau, \tag{5}$$

where $\boldsymbol{\eta} = (\xi, \eta, \zeta)$ is a source separation vector from one source location to another and $\Delta\tau$ is the time delay between the two sources. The source terms on the right hand side are

$$\Theta_0 = -\frac{\partial \underline{\rho}}{\partial t} - \frac{\partial \underline{\rho}\underline{u}_j}{\partial x_j}, \tag{6}$$

$$\Theta_i = -\frac{\partial \underline{\rho}\underline{u}_i}{\partial t} - \frac{\partial \underline{\rho}\underline{u}_i\underline{u}_j}{\partial x_j} - \frac{\partial \underline{p}}{\partial x_j}\delta_{ij} + \frac{\partial}{\partial x_j}\left[\mu\left(\frac{\partial \underline{u}_i}{\partial x_j} + \frac{\partial \underline{u}_j}{\partial x_i}\right)\right] - \frac{2}{3}\frac{\partial}{\partial x_j}\left[\mu\frac{\partial \underline{u}_k}{\partial x_k}\right], \tag{7}$$

and

$$\Theta_4 = -\frac{\partial \underline{p}}{\partial t} - \frac{\gamma-1}{2}\frac{\partial \underline{\rho}\underline{u}_k\underline{u}_k}{\partial t} - \gamma\frac{\partial \underline{u}_j\underline{p}}{\partial x_j} - \frac{\gamma-1}{2}\frac{\partial \underline{\rho}\underline{u}_j\underline{u}_k\underline{u}_k}{\partial x_j} + (\gamma-1)\frac{\partial}{\partial x_j}\left[\frac{c_p\mu}{Pr}\frac{\partial \underline{T}}{\partial x_j}\right] + (\gamma-1)\frac{\partial}{\partial x_j}\left[\mu\underline{u}_i\left(\frac{\partial \underline{u}_i}{\partial x_j} + \frac{\partial \underline{u}_j}{\partial x_i}\right)\right]$$

$$-\frac{2}{3}(\gamma-1)\delta_{ij}\frac{\partial}{\partial x_j}\left[\mu\underline{u}_i\frac{\partial \underline{u}_k}{\partial x_k}\right], \tag{8}$$

where Θ_0 represents the source terms from the continuity equation, Θ_i (where $i = 1,2,3$) represents the three components of the source terms from the momentum equations, and Θ_4 represents the source terms from the energy equation. To obtain the acoustic pressure spectrum, we rewrite Eq. (1) for pressure as

$$S_4^{\perp}(\mathbf{x},\omega) = \int_{-\infty}^{\infty}\cdots\int_{-\infty}^{\infty}\sum_{m=0}^{4}\sum_{n=0}^{4}\tilde{p}_g^{*\perp,m}(\mathbf{x};\mathbf{y},\omega)\tilde{p}_g^{\perp,n}(\mathbf{x};\mathbf{y}+\boldsymbol{\eta},\omega)R_{m,n}^{\perp}(\mathbf{y},\boldsymbol{\eta},\tau)\exp\left[i\omega\tau\right]d\tau d\boldsymbol{\eta}d\mathbf{y}. \tag{9}$$

B. Vector Green's Function

To derive the vector Green's function, we assume that the environment is quiescent as the refraction effects of the shear layer are negligible for BBSAN [32–34]. The viscous effects on the linear sound propagation are also ignored [35]. We use the relation $\gamma p_\infty = c_\infty^2\rho_\infty$, multiply c_∞^2 on the gradient of the momentum vector Green's function Eq. (4), and subtract the result from the time derivative of the energy vector Green's function Eq. (3). We obtain

$$\frac{\partial^2 p_g^{\perp n}}{\partial t^2} - c_\infty^2\frac{\partial^2 p_g^{\perp n}}{\partial x_i^2} = \frac{\partial}{\partial t}\left[\delta(\mathbf{x}-\mathbf{y})\delta(t-\tau)\delta_{4n}\right] - c_\infty^2\frac{\partial}{\partial x_i}\left[\delta(\mathbf{x}-\mathbf{y})\delta(t-\tau)\delta_{in}\right]. \tag{10}$$

Performing the Fourier transform with respect to time on Eq. (10) we obtain

$$\omega^2\tilde{p}_g^{\perp n} + c_\infty^2\frac{\partial^2\tilde{p}_g^{\perp n}}{\partial x_i^2} = i\omega\delta(\mathbf{x}-\mathbf{y})\delta_{4n} + c_\infty^2\frac{\partial}{\partial x_i}\delta(\mathbf{x}-\mathbf{y})\delta_{in}. \tag{11}$$

The solution to the vector Green's function for pressure in the far-field is

$$\tilde{p}_g^{\perp n}(\mathbf{x},\mathbf{y},\omega) = \frac{i\omega}{4\pi c_\infty r}\exp\left[\frac{i\omega r}{c_\infty}\right]\left(\frac{x_i}{r}\delta_{in} - \frac{1}{c_\infty}\delta_{4n}\right), \tag{12}$$

where $r = |\mathbf{x}-\mathbf{y}|$. Note that the value of the Kronecker delta function δ_{ij} is 1 only if $i = j$, and is 0 if $i \neq j$. Following Tam and Auriault [36], we obtain

$$\tilde{p}_g^{\perp n}(\mathbf{x},\mathbf{y}+\boldsymbol{\eta},\omega) = \tilde{p}_g^{\perp n}(\mathbf{x},\mathbf{y},\omega)\exp\left[-\frac{i\omega\mathbf{x}\cdot\boldsymbol{\eta}}{c_\infty r}\right], \tag{13}$$

which is a relation for the phase difference between two streamwise source locations within a jet after the far-field assumption has been made. Next, we identify the source terms for BBSAN.

C. Source Term for BBSAN

The source term in Eq. (9) is the two-point cross-correlation of the sources of Eqs. (6) to (8). The two-point cross-correlation is denoted by $R_{m,n}^{\perp}$, where m and n ranges from 0 to 4 corresponding to the continuity, momentum, and energy equations. $R_{0,0}^{\perp}$ represents the two-point cross-correlation of the continuity equation with itself, $R_{0,1}^{\perp}$ to $R_{0,3}^{\perp}$ represents the two-point cross-correlation of the continuity equation with the three components of the momentum equations, while $R_{0,4}^{\perp}$ represents the two-point cross-correlation of the continuity equation with the energy equation. Similarly, other terms represent the two-point cross-correlation of the momentum equations with the continuity and energy equation, and energy equation with the continuity and momentum equations.

As an example, the two-point cross-correlation for the continuity-continuity equation can be written as

$$R_{0,0}^{\perp} = \langle\Theta_0(\mathbf{y},\tau),\Theta_0(\mathbf{y}+\boldsymbol{\eta},\tau+\Delta\tau)\rangle = \left\langle\left(-\frac{\partial\underline{\rho}^{(1)}}{\partial\tau} - \frac{\partial\underline{\rho}^{(1)}\underline{u}_j^{(1)}}{\partial y_j}\right),\left(-\frac{\partial\underline{\rho}^{(2)}}{\partial\tau} - \frac{\partial\underline{\rho}^{(2)}\underline{u}_m^{(1)}}{\partial y_m}\right)\right\rangle. \tag{14}$$

Expanding Eq. (14), we can write the two-point cross-correlation as

$$R_{0,0}^{\perp}(\mathbf{y},\boldsymbol{\eta},\tau) = \left\langle\frac{\partial\underline{\rho}^{(1)}}{\partial\tau},\frac{\partial\underline{\rho}^{(2)}}{\partial\tau}\right\rangle + \left\langle\frac{\partial\underline{\rho}^{(1)}}{\partial\tau},\frac{\partial\underline{\rho}^{(2)}\underline{u}_m^{(2)}}{\partial y_m}\right\rangle + \left\langle\frac{\partial\underline{\rho}^{(1)}\underline{u}_j^{(1)}}{\partial y_j},\frac{\partial\underline{\rho}^{(2)}}{\partial\tau}\right\rangle + \left\langle\frac{\partial\underline{\rho}^{(1)}\underline{u}_j^{(1)}}{\partial y_j},\frac{\partial\underline{\rho}^{(2)}\underline{u}_m^{(2)}}{\partial y_m}\right\rangle. \tag{15}$$

Expanding the two-point cross-correlation terms for all possible sources will result in 576 terms. In Eqs. (14) and (15), the superscripts (1) and (2) denote the location of two different source terms, one at location $\mathbf{y}$ and the other at $\mathbf{y} + \boldsymbol{\eta}$. We can further decompose each term of Eq. (15) into the base flow quantity, isotropic fluctuations, and anisotropic fluctuations. One of the terms within the energy-energy correlation can be decomposed to 6561 further terms. Evaluating each individual term is tedious. To find the BBSAN source term within all possible source term expansions, we eliminate various source terms that do not correlate with the scaling of BBSAN.

Lighthill [37] showed that the effect of viscous terms on noise generation is very small compared to other source terms. Hence, the effect of viscous source terms for BBSAN can be neglected. This drastically reduces the number of terms to be evaluated. The remaining source terms in the momentum and energy equations are written as

$$\Theta_i = -\frac{\partial \underline{\rho}\underline{u_i}}{\partial t} - \frac{\partial \underline{\rho}\underline{u_i}\underline{u_j}}{\partial x_j} - \frac{\partial \underline{p}}{\partial x_j}\delta_{ij} \tag{16}$$

and

$$\Theta_4 = -\frac{\partial \underline{p}}{\partial t} - \frac{\gamma-1}{2}\frac{\partial \underline{\rho}\underline{u_k}\underline{u_k}}{\partial t} - \gamma\frac{\partial \underline{u_j}\underline{p}}{\partial x_j} - \frac{\gamma-1}{2}\frac{\partial \underline{\rho}\underline{u_j}\underline{u_k}\underline{u_k}}{\partial x_j}. \tag{17}$$

Some of the terms are further eliminated using the statistical properties of the cross-correlation function. The third term in Eq. (16) and the first term in Eq. (17), i.e. gradient of pressure and the time derivative of pressure are eliminated and are not candidates for BBSAN. As the time derivative and spatial derivative of mean quantities is zero and a constant, respectively, the two-point cross-correlation of both these terms with any of the other remaining terms are zero. Similarly, the first term in Eq. (16) and the second term in Eq. (17) can be eliminated as both involve time derivative terms. A scaling analysis of the remaining terms with the off-design parameter β, was performed by Patel and Miller [30] to ascertain the source term for BBSAN. The only two-point cross-correlation source term that scales as β^4 in the sideline direction for a cold jet is

$$R^{(4)} = \gamma^2 \left\langle \hat{u}_j^{(1)} \frac{\partial \overline{p}^{(1)}}{\partial y_j}, \hat{u}_m^{(2)} \frac{\partial \overline{p}^{(2)}}{\partial y_m} \right\rangle, \tag{18}$$

where $\hat{\boldsymbol{u}}$ represents the coherent anisotropic large-scale structures and the gradient of mean pressures represent the shock-structure. Hence, the multiplication of the anisotropic velocity with the gradient of mean pressure represents the interaction between the large-scale turbulent structures with the shock-cell structures, which is the source of BBSAN.

We model Eq. (18) instead of performing an expensive LES or direct numerical simulation (DNS) to obtain the cross-correlation of the BBSAN source terms at two different locations. Following Ribner [38], we model these two-point cross-correlation terms as

$$R^{\perp}_{m,n} = \mathcal{A}R, \tag{19}$$

where $\mathcal{A}$ represents the magnitude of the two-point cross-correlation source term and R represents the normalized two-point cross-correlation term. The magnitude is directly obtained from the source term, while the normalized two-point cross-correlation term is modeled based on theoretical or experimental results. Note that the normalized two-point cross-correlation term will be different depending on whether the source term is isotropic, anisotropic, or is an interaction of the large-scale turbulence with the fine-scale turbulence. We model Eq. (18) using Eq. (19) and obtain

$$R^{(4)} = \gamma^2 \frac{\partial \overline{p}^{(1)}}{\partial y_j}\frac{\partial \overline{p}^{(2)}}{\partial y_m}\hat{u}_j^{(1)}\hat{u}_m^{(2)}\hat{R}. \tag{20}$$

Ribner [38] modeled the normalized two-point cross-correlation as

$$\hat{R} = \exp\left[-\frac{|\tau|}{\tau_s}\right]\exp\left[-\frac{(\xi - u_c\tau)^2}{l^2}\right]\exp\left[-\frac{(\eta^2+\zeta^2)}{l_\perp^2}\right], \tag{21}$$

where τ_s is the time scale, l and $l_\perp$ are the length scales in the streamwise and cross-stream direction, respectively, and u_c is the eddy convection speed.

D. Evaluation of the Spectral Density

We substitute the source terms modeled in Eqs. (20) and (21), and the solution to the vector Green's function of Eqs. (12) and (13) in Eq. (9), and integrate the resulting equation with respect to τ and $\boldsymbol{\eta}$. We follow the approach of Morris and Miller [7] to evaluate the gradient of pressure at two different locations. The resulting spectral density is very similar to the model of Morris and Miller [7] because we use the same normalized two-point cross-correlation model. However, the source terms in both models are different. After integrating, we obtain

$$S_4^{\perp}(\mathbf{x},\omega) = \frac{\gamma^2\omega^2}{16\pi\sqrt{\pi}c_\infty^4 r^2}\iiint_{-\infty}^{\infty} l_\perp^2 l\tau_s \exp\left[-\frac{\omega^2 l_\perp^2 \sin^2\theta}{4c_\infty^2}\right]\frac{\partial\overline{p}}{\partial y_j}(\mathbf{y})\hat{u}_j(\mathbf{y})$$
$$\times\left[\int_{-\infty}^{\infty}\frac{\exp\left[-l^2\left(\kappa-\frac{\omega\cos\theta}{c_\infty}\right)^2/4\right]}{\left[1+\left(1-M_c\cos\theta+\frac{u_c\kappa}{\omega}\right)^2\omega^2\tau_s^2\right]}\frac{\partial\overline{p}}{\partial y_m}(\kappa,y_2,y_3)d\kappa\right]\cdot\hat{u}_m(\mathbf{y})d\mathbf{y}, \tag{22}$$

where κ is the wavenumber, $M_c = u_c c_\infty^{-1}$ represents the convective Mach number, and θ is the polar observer angle. The implementation of Eq. (22) is performed similar to Morris and Miller [7].

The mean values used to evaluate Eq. (22) are obtained using the steady RANS CFD simulations, while the isotropic and anisotropic fluctuations are modeled based on theoretical and experimental results. The RANS simulation is closed using the Menter [39] $K-\Omega$ shear stress transport (SST) model, where K represents the turbulent kinetic energy and Ω represents the specific dissipation rate. The Fully Unstructured Navier-Stokes (FUN3D) [40] CFD code developed at NASA Langley Research Center is used to calculate the solution to the RANS equations. The convection velocity of large-scale turbulent structures is modeled as $u_c = \overline{u}$. The dissipation rate ϵ is obtained using $\epsilon = 0.09K\Omega$. A length scale and time scale are estimated from turbulent kinetic energy and dissipation rate as $l = c_l K^{3/2}\epsilon^{-1}$, $l_\perp = c_\perp l$, and $\tau_s = c_\tau K\epsilon^{-1}$, where c_τ, c_l, and $c_\perp$ are constants.

Pope [41] modeled the composite energy spectrum for velocity based on Kolmogorov [42] self-similarity spectrum in the inertial subrange as

$$E_u(\kappa) = c_u\epsilon^{2/3}\kappa^{-5/3}f_{L,u}(\kappa L)f_{\eta,u}(\kappa\eta), \tag{23}$$

where the constant $c_u = 1.5$. The spectrum scales as $\kappa^{-5/3}$ in the inertial subrange region, and is connected to the energy containing range and the dissipation range by the composite spectrum proposed by Pope [41] as

$$f_{L,u}(\kappa L) = \left[\frac{\kappa L}{\sqrt{(\kappa L)^2+6.78}}\right]^{11/3} \tag{24a}$$

and

$$f_{\eta,u}(\kappa\eta) = \exp\left[-2.1\left(\left[(\kappa\eta)^4+0.0256\right]^{1/4}-0.4\right)\right]. \tag{24b}$$

The anisotropic velocities are modeled based on the numerical and theoretical work of Ishihara et al. [43]. They showed that the anisotropic energy spectrum for velocity in the homogeneous turbulent shear layer scales as

$$\hat{E}_u(\kappa) = c_u\epsilon^{1/3}\kappa^{-7/3}f_{L,u}(\kappa L)f_{\eta,u}(\kappa\eta). \tag{25}$$

The amplitude in the energy containing range for anisotropic spectra is matched with Kolmogorov [42] theory. The isotropic spectrum is estimated by subtracting the anisotropic spectrum from the total velocity spectrum. The anisotropic velocity can be obtained from the energy spectrum as

$$\hat{u}_i(\mathbf{y},\tau) = \left[\frac{2}{3}\int_{\kappa_1}^{\kappa_2}\hat{E}_u(\mathbf{y},\kappa,\tau)d\kappa\right]^{1/2}. \tag{26}$$

The limits of the integrations, κ_1 and κ_2, are determined based on the frequency that is being evaluated. The wavenumber is related to the frequency as $\kappa = \omega c_\infty^{-1}$.

Validation of the model with the experimental small hot jet acoustic rig (SHJAR) database [44] has been performed by Patel and Miller [30] for different jet operating conditions and observer angles. In Section III, we perform a numerical sensitivity analyses of the shock-associated noise by perturbing various parameters.

III. Sensitivity Analysis

A. Sensitivity Analyses of the Model Parameters

The sensitivity analyses of BBSAN on various model parameters such as length and time scales, gradient of pressure, anisotropic velocities, and convective velocity is performed. We vary the model parameters by 1% for the sensitivity analyses. The change in the sound pressure level per unit Strouhal number from Eq. (22) is calculated. The arguments to the model developed in Eq. (22) are obtained using RANS CFD calculations. The nozzle used for the CFD calculations is the SMC016 nozzle, where SMC stands for small metal chevron. SMC016 is an axisymmetric convergent-divergent nozzle designed using method of characteristics (MOC) having a design Mach number, $M_d = 1.5$.

The domain and the boundary conditions used for the CFD calculations are shown in Fig. 2, while the computational mesh is shown in Fig. 3. The computational domain is extended to $100D$ in the downstream direction and $50D$ in the cross-stream direction, where $D = 0.0508$ m is the diameter of the nozzle exit. As the nozzles are axisymmetric, the generated 2D mesh is extruded by rotating it 90° in the azimuthal direction. Symmetric plane boundary conditions are applied on the $x - y$ and $x - z$ planes to save computational expense. The gradient of the field-variables normal to the plane are set to zero for symmetric plane boundary conditions. The total pressure and total temperature are specified at the inlet of the nozzles, a pressure outlet specified as atmospheric pressure is set at the exit of the computational domain, an adiabatic no-slip wall is specified at the nozzle walls, and a zero free-stream velocity is specified on the top and side boundary of the domain.

The sensitivity analyses of various model parameters is shown in Fig. 4 for an unheated jet case having an NPR = 5.2 for the observer in the sideline direction ($\theta = 90°$). All the parameters inside the model are varied by 1% while keeping other parameters constant. The SPL at each Strouhal number is calculated based on the model. The experimental noise spectrum corresponding to NPR = 5.2 and TTR = 1.0 from the SHJAR database is superposed in Fig. 4 along with the sensitivity results. We observe that sensitivity of all the parameters is less than 0.1 dB for the peak BBSAN. The sensitivity of the convective velocity is the highest among all the parameters. The sensitivity of all other parameters is less than 1 dB for all Strouhal numbers.

The sensitivity of length scale in streamwise direction, time scale, and convective velocity is high at the trough between two BBSAN spectral peaks. However, the sensitivity decreases for all three parameters at the BBSAN peaks. The sensitivity of gradient of mean pressure and the anisotropic velocities is constant for all the Strouhal numbers. The SPL varies by 0.1 dB with 1% change in either the gradient of mean pressure or the anisotropic velocities. Since the product of the gradient of mean pressure and the anisotropic velocities is the source term for BBSAN, any change in the parameters of the source term directly affects the sound radiated from the model. We now study the effect of different nozzle geometries and jet operating condition on the BBSAN.

B. Effect of Nozzle Geometry

The sensitivity of shock-associated noise on different parameters such as the NPR, TTR, area ratio, and the boundary layer is performed using the identified source term and the model developed in Eqs. (18) and (22), respectively. We perform the sensitivity analysis of BBSAN using the SMC016 nozzle and a biconic nozzle. Both the nozzles are axisymmetric convergent-divergent nozzles with design Mach number $M_d = 1.50$. The biconic nozzle is chosen because its shape is more representative of a low bypass military engine nozzle. We select the operating conditions from the SHJAR database [44] developed by NASA Glenn Research Center.

Both the nozzles are operated over a range of conditions from NPR = 2.4 to 6.0 for an unheated jet with TTR = 1.0. The RANS CFD simulations are performed at NPR = [2.4, 2.75, 3.1, 3.382, 3.503, 3.593, 3.643] for over-expanded conditions and are performed at NPR = [3.693, 3.745, 3.858, 4.043, 4.32, 4.7, 5.2, 6.0] for under-expanded conditions. The BBSAN intensity versus the fully-expanded jet Mach number for different operating conditions is plotted in Fig. 5. The BBSAN intensity is minimum at the design condition for the SMC016 nozzle and is consistent with the experimental results of Tam and Tanna [3]. However, very little reduction of noise is observed for the biconic nozzle at the design condition. The BBSAN intensity remains almost constant near the design condition and increases with increasing NPR for the biconic nozzle.

A comparison of the Mach number contours from the SMC016 nozzle with the biconic nozzle is shown in Fig. 6. Both the nozzles are operating at a design condition corresponding to NPR = 3.67 and TTR = 1.0. The SMC016 nozzle is an MOC nozzle, and the reflection of the characteristics from the nozzle wall are eliminated. Hence, no shocks are observed in the exhaust of the jet for the SMC016 nozzle. However, we observe a shock-cell structure in the jet exhaust for the biconic nozzle in Fig. 6. The biconic nozzle contains an abrupt change from the convergent section to the

divergent section. This abrupt change causes shocks to form within the nozzle. Because of this, an additional shock-cell structure is observed for biconic nozzles, and the BBSAN is observed at the on-design condition. The noise for the SMC016 nozzle is reduced at the design condition, while the noise remains almost constant for the biconic nozzle. The noise for the SMC016 nozzle at the design condition reduces by 10 dB relative to the biconic nozzle at the same operating condition. The source term intensity of the SMC016 nozzle at the design condition is reduced by 96% when compared with the biconic nozzle.

C. Effect of Jet Operating Conditions

A numerical sensitivity analyses is performed by perturbing the NPR, TTR, and area ratio for unheated jet cases using an SMC016 nozzle and heated jet cases using a biconic nozzle. The NPR and TTR are perturbed by 1% by changing the boundary conditions in the RANS simulations. To perturb the area ratio by 1%, new nozzle contours are designed. Perturbation of the area ratio for the biconic nozzle is performed by joining a straight line from the nozzle throat to the perturbed nozzle exit. For the SMC016 nozzle case, we use an MOC tool developed by Rice [45] to design a MOC nozzle with 1% increased or decreased area ratio. The perturbed MOC nozzle contours are compared with the baseline SMC016 nozzle in Fig. 7.

The plots of the source intensity of the BBSAN against the fully-expanded jet Mach number for the SMC016 nozzle are shown in Figs. 8(a), 8(c), and 8(e) for perturbed NPR, TTR, and area ratio, respectively. The corresponding change in the peak SPL with the perturbed quantities are shown in Figs. 8(b), 8(d), and 8(f), respectively. The shaded regions in Fig. 8 denotes the difference between the perturbed case and the base case. For a convergent-divergent nozzle designed using MOC, the minimum intensity is observed at the on-design condition and the intensity increases as β^4 with variation of the NPR from the on-design condition. Formation of the Mach disks in the jet exhaust at moderately over- and under-expanded conditions changes the scaling of BBSAN with β^4. These characteristics are observed in Fig. 8, and are consistent with the experimental results of Tanna [9].

As BBSAN is the most dominant component in the sideline direction when the jet is operating at slightly imperfectly expanded conditions, the sensitivity with perturbed input parameters is most apparent in this direction. The maximum sensitivity of BBSAN with NPR, TTR, and area ratio are 70.41%, 1.48%, and 237.17%, respectively for the SMC016 nozzle. Correspondingly, the maximum change in the SPL with perturbation in NPR, TTR, and area ratio is 3.27 dB, 0.13 dB, and 6.2 dB respectively. BBSAN is the most sensitive to the area ratio and the least sensitive to the TTR [17], as observed from Figs. 8(c) to 8(f), respectively.

Figure 8(a) shows that increasing the NPR by 1% from the base case decreases the intensity of BBSAN at over-expanded conditions. Correspondingly, the SPL also decreases as seen in Fig. 8(b). However, at under-expanded conditions, increasing the NPR by 1% increases the intensity and SPL. This is because it moves closer to the design condition in the former case, while it moves away from the design condition in the later case. For an unheated jet, Figs. 8(c) and 8(d) shows that perturbing the TTR does not have any major effect on the intensity of BBSAN. Changing the area ratio by 1% changes the design Mach number of the nozzle. Increasing and decreasing the area ratio by 1% changes the design Mach number of the nozzle to 1.517 and 1.482, respectively. This is observed in Fig. 8(e), where the minimum intensity shifts either to the left or right side of the base case, depending whether the area ratio is increased or decreased. Figure 8(f) shows that the SPL decreases for over-expanded conditions by 4 dB and increases by 6.2 dB for under-expanded conditions when the area ratio is decreased. If the area ratio is increased, the SPL increases by 5 dB for over-expanded conditions and reduces by 2 dB for under-expanded conditions.

The sensitivity analyses plots at different fully-expanded jet Mach numbers for the biconic nozzle at heated conditions are shown in Fig. 9 for perturbed NPR, TTR, and area ratio. The sensitivity for all perturbed parameters are less in comparison to the SMC016 nozzle at unheated jet conditions. The maximum sensitivity with perturbed NPR is 46.56% at the NPR = 2.4, as observed in Fig. 9(a). Correspondingly, the SPL is increased by 1.15 dB at the same NPR in Fig. 9(b). At this NPR, separation of flow inside the nozzle is observed. Excluding this operating condition, the maximum sensitivity with perturbed NPR is 20.22% at NPR = 2.75, as seen in Fig. 9(a). Figure 9(b) shows that the maximum change in the SPL is less than 0.5 dB for all the jet operating conditions.

Similar to the SMC016 nozzle operating at unheated jet conditions, perturbing the TTR does not have a major effect on the BBSAN intensity for the biconic nozzles at heated jet conditions. The source term intensity varies by a maximum of 0.36% and the SPL varies by a maximum of 0.2 dB, as observed in Figs. 9(c) and 9(d), respectively. The maximum sensitivity with perturbed area ratio is observed to be 21.32% at NPR = 4.32 for the biconic nozzle case shown in Fig. 9(e). Figure 9(f) shows that the SPL varies by a maximum of 1.5 dB when the area ratio is perturbed. A shock-cell structure is always present for the biconic nozzle. Hence, the reduction of noise does not happen as rapidly at

the design condition as the MOC designed nozzle. Hence, for all the perturbed parameters, the unheated SMC016 nozzle is found to be more sensitive compared to the heated biconic nozzle.

We also examine the effect of source location when various input conditions are perturbed. The source location corresponding to the maximum intensity of the source term at the peak Strouhal number are plotted in Fig. 10. Figures 10(a), 10(c), and 10(e) shows the source location in the streamwise direction for the SMC016 nozzle and Figs. 10(b), 10(d), and 10(f) shows the source location in the streamwise direction for the biconic nozzle. We observe that the source locations shift downstream from $x/D = 3.66$ to $x/D = 8.41$ for the SMC016 nozzle and from $x/D = 3.00$ to $x/D = 9.07$ for the biconic nozzle, when the fully-expanded jet Mach number is increased from $M_j = 1.19$ to $M_j = 1.82$. The over-expanded cases have shorter potential core length, and the shock-cell spacing is also smaller relative to under-expanded cases. Hence, the source locations are far from the nozzle for the under-expanded cases relative to the over-expanded cases. However, for all cases, the maximum source term is found in between the fourth to sixth shock-cells.

The source location shifts upstream for the SMC016 nozzle operating at the design condition. As very weak shocks are observed for the design condition, the BBSAN is not dominant for this condition. The source location moves approximately by $0.1D$ for all the cases when the NPR is perturbed by 1%, as observed in Figs. 10(a) and 10(b) for the SMC016 nozzle and the biconic nozzle, respectively. We also observe from the Figs. 10(c) and 10(d) that the shock-locations do not change with variation of TTR. Hence, the axial source locations also do not vary with perturbation in TTR. Figures 10(e) and 10(f) shows the variation in source locations for the SMC016 nozzle and the biconic nozzle when the area ratio is perturbed. The axial source location moves by $2.5D$ near the design condition for the SMC016 nozzle when the area ratio is perturbed. For the biconic nozzle, very little change in the source location is observed with small perturbation in the area ratio. The axial source location shifts by $0.05D$ for most operating conditions for the biconic nozzle as observed in Fig. 10(f). Note that we have not plotted sources at adjacent locations because Fig. 10 are representative results.

D. Effect of Boundary Layer Variation at Nozzle Exit

In this section, we investigate the effect of the boundary layer on the BBSAN intensity. Three different methods are used to alter the boundary layer at the exit of the nozzle. The extension of the converging section, a forward step at the inlet, and a backward step at the inlet are used to modify the boundary layer at the exit of the nozzle. The forward and backward steps offer less control of the boundary layer thickness at the nozzle exit. The thickness of the boundary layer can be precisely controlled by varying the length of the converging section of the nozzle. This approach is similar to Zaman [22]. The thickness of the turbulent boundary layer for a flat plate scales as $xRe_x^{-1/5}$, where x is the downstream distance. Hence, a long converging section is required to obtain a large boundary layer thickness at the exit. However, extending the length of the nozzle increases the number of grid points in the domain and the computational expense increases.

All three cases are simulated using the unheated SMC016 nozzle operating at NPR = 5.2 and TTR = 1.0. The converging section is extended by $9D$ for the extended length case, and a step height of $0.03D$ is used for the forward and backward steps. The non-dimensionalized velocity is plotted against the non-dimensionalized distance from the wall in Fig. 11(a) using the inner co-ordinates. The non-dimensionalized mean-velocity and turbulent kinetic energy in the outer co-ordinates are plotted in Fig. 11(b). The thickness of the boundary layer is the largest for the backward facing step as observed from Fig. 11(b). Using Eq. (22), we also find that the maximum reduction of noise is observed for the backward facing step. Hence, we use the backward facing step for evaluating the reduction of the source term intensity at different operating conditions.

We simulate different operating conditions using the backward facing step for both the nozzles. Figure 12(a) shows the reduction of source term intensity due to the variation of the statistics of the turbulent boundary layer. The solid lines represent the base case, and the dashed lines represent the backward facing step. The maximum reduction in noise for the SMC016 nozzle is observed at NPR = 3.858, and the intensity of the noise is reduced by 41.62%. However, the maximum reduction in the biconic nozzle is 2.07%, which is observed at the on-design condition. The maximum change in the SPL for an SMC016 nozzle is 2.5 dB as shown in Fig. 12(b). We observe that the SPL increases with increasing boundary layer thickness for the over-expanded cases. This increase is likely due to a reduced effective exit area of the nozzle, thus increasing the noise. However, the SPL for the biconic nozzle varies less than 0.1 dB for all the jet conditions except at NPR = 2.4. The abrupt change between the converging and diverging sections induces additional turbulence in the boundary layer, and relatively less reduction of the source term intensity is observed.

IV. Summary and Conclusions

A decomposition based on the Navier-Stokes equations has been used to identify the source term responsible for BBSAN. The source term responsible for BBSAN consists of the product of the gradient of mean pressure and the anisotropic velocities. The gradient of mean pressure represents the shock-strength and the anisotropic velocities represent the large-scale turbulent fluctuations. A closed-form model is developed using the source term responsible for BBSAN. A RANS model is used for evaluating the mean values, while numerical and theoretical results are used to evaluate the fluctuating quantities in the model.

A sensitivity analyses of the parameters of the model has been performed. We observed that for the peak SPL, the sensitivity of all parameters was less than 0.1 dB. At other Strouhal numbers, the convection velocity was observed to be the most sensitive. The gradient of mean pressure and the anisotropic velocities directly affected the SPL at all Strouhal numbers. The developed model is used for sensitivity analyses of BBSAN by perturbing different jet operating parameters such as NPR, TTR, and nozzle area ratio. Among the three parameters evaluated for sensitivity analyses, the most sensitive operating parameter is the area ratio, while the least sensitive parameter is the TTR. The biconic nozzle is relatively less sensitive to all the operating parameters compared to the SMC016 nozzle. Reduction of noise with thicker boundary layer profile has been observed for the SMC016 nozzle at under-expanded conditions. However, very little change of SPL is observed for the biconic nozzle.

Acknowledgements

This research was supported by the Office of Naval Research Grant N00014-17-1-2583. Any opinions, findings, and conclusions or recommendations expressed in this material are those of the author(s) and do not necessarily reflect the views of the Office of Naval Research.

References

[1] Doychak, J., "Department of Navy Jet Noise Reduction Project Overview," *15th Annual Partners in Environmental Technology Technical Symposium and Workshop*, Washington D.C., 2010. URL https://apps.dtic.mil/dtic/tr/fulltext/u2/a553981.pdf.

[2] Harper-Bourne, M., and Fisher, M. J., "The Noise from Shocks Waves in Supersonic Jets," *NATO AGARD-CP-131*, Vol. 11, 1973, pp. 1–13.

[3] Tam, C. K. W., and Tanna, H. K., "Shock Associated Noise of Supersonic Jets from Convergent-Divergent Nozzles," *Journal of Sound and Vibration*, Vol. 81, No. 3, 1982, pp. 337–358. doi:10.1016/0022-460X(82)90244-9.

[4] Tam, C. K. W., "Stochastic Model Theory of Broadband Shock Associated Noise from Supersonic Jets," *Journal of Sound and Vibration*, Vol. 116, No. 2, 1987, pp. 265–302. doi:10.1016/S0022-460X(87)81303-2.

[5] Tam, C. K. W., and Chen, K. C., "A Statistical Model of Turbulence in Two-Dimensional Mixing Layers," *Journal of Fluid Mechanics*, Vol. 92, No. 02, 1979, pp. 303–326. doi:10.1017/S002211207900063X.

[6] Pack, D. C., "A Note on Prandtl's Formula for the Wave-Length of a Supersonic Gas Jet," *The Quarterly Journal of Mechanics and Applied Mathematics*, Vol. 3, No. 2, 1950, pp. 173–181. doi:10.1093/qjmam/3.2.173.

[7] Morris, P. J., and Miller, S. A. E., "Prediction of Broadband Shock-Associated Noise Using Reynolds-Averaged Navier-Stokes Computational Fluid Dynamics," *AIAA Journal*, Vol. 48, No. 12, 2010, pp. 2931–2944. doi:10.2514/1.J050560.

[8] Suzuki, T., "Wave-Packet Representation of Shock-Cell Noise for a Single Round Jet," *AIAA Journal*, Vol. 54, No. 12, 2016, pp. 3903–3917. doi:10.2514/1.J055097.

[9] Tanna, H. K., "An Experimental Study of Jet Noise Part II: Shock Associated Noise," *Journal of Sound and Vibration*, Vol. 50, No. 3, 1977, pp. 429–444. doi:10.1016/0022-460X(77)90494-1.

[10] Seiner, J. M., and Norum, T. D., "Experiments of Shock Associated Noise of Supersonic Jets," *12th Fluid and Plasma Dynamics Conference*, AIAA Paper No. 79-47341, Reston, Virigina, 1979. doi:10.2514/6.1979-1526.

[11] Seiner, J. M., and Norum, T. D., "Aerodynamic Aspects of Shock Containing Jet Plumes," *6th Aeroacoustics Conference*, AIAA Paper No. 80-43600, Reston, Virigina, 1980. doi:10.2514/6.1980-965.

[12] Norum, T. D., and Seiner, J. M., "Location and Propagation of Shock Associated Noise from Supersonic Jets," *AIAA 6th Aeroacoustics Conference*, AIAA Paper No. 80-43599, Reston, Virigina, 1980. doi:10.2514/6.1980-983.

[13] Norum, T. D., and Seiner, J. M., "Measurements of Mean Static Pressure and Far-Field Acoustics of Shock-Containing Supersonic Jets," *NASA/TM-84521 19820025274*, 1982.

[14] Norum, T. D., and Seiner, J. M., "Broadband Shock Noise from Supersonic Jets," *AIAA Journal*, Vol. 20, No. 1, 1982, pp. 68–73. doi:10.2514/3.51048.

[15] Seiner, J. M., and Yu, J. C., "Acoustic Near-Field Properties Associated with Broadband Shock Noise," *AIAA Journal*, Vol. 22, No. 9, 1984, pp. 1207–1215. doi:10.2514/3.8762.

[16] Bridges, J. E., and Wernet, M. P., "Turbulence Associated With Broadband Shock Noise in Hot Jets," *NASA/TM-2008-215274*, , No. September 2008, 2008.

[17] Viswanathan, K., Alkislar, M. B., and Czech, M. J., "Characteristics of the Shock Noise Component of Jet Noise," *AIAA Journal*, Vol. 48, No. 1, 2010, pp. 25–46. doi:10.2514/1.38521.

[18] Kuo, C.-W., McLaughlin, D. K., Morris, P. J., and Viswanathan, K., "Effects of Jet Temperature on Broadband Shock-Associated Noise," *AIAA Journal*, Vol. 53, No. 6, 2015, pp. 1515–1530. doi:10.2514/1.J053442.

[19] Miller, S. A. E., "The Scaling of Broadband Shock-Associated Noise with Increasing Temperature," *International Journal of Aeroacoustics*, Vol. 14, No. 1-2, 2015, pp. 305–326. doi:10.1260/1475-472X.14.1-2.305.

[20] Mabe, J., "Variable Area Jet Nozzle for Noise Reduction Using Shape Memory Alloy Actuators," *The Journal of the Acoustical Society of America*, Vol. 123, No. 5, 2008, pp. 3871–3871.

[21] Michel, U., "The Benefits of Variable Area Fan Nozzles on Turbofan Engines," *49th AIAA Aerospace Sciences Meeting*, American Institute of Aeronautics and Astronautics, Reston, Virigina, 2011. doi:10.2514/6.2011-226.

[22] Zaman, K. B. M. Q., "Effect of Initial Boundary-Layer State on Subsonic Jet Noise," *AIAA Journal*, Vol. 50, No. 8, 2012, pp. 1784–1795. doi:10.2514/1.J051712.

[23] Bogey, C., and Bailly, C., "Influence of Nozzle-Exit Boundary-Layer Conditions on the Flow and Acoustic Fields of Initially Laminar Jets," *Journal of Fluid Mechanics*, Vol. 663, 2010, pp. 507–538. doi:10.1017/S0022112010003605.

[24] Bogey, C., Marsden, O., and Bailly, C., "Large-Eddy Simulation of the Flow and Acoustic Fields of a Reynolds Number 10^5 Subsonic Jet with Tripped Exit Boundary Layers," *Physics of Fluids*, Vol. 23, No. 3, 2011, p. 035104. doi:10.1063/1.3555634.

[25] Brès, G. A., Jordan, P., Jaunet, V., Le Rallic, M., Cavalieri, A. V. G., Towne, A., Lele, S. K., Colonius, T., and Schmidt, O. T., "Importance of the Nozzle-Exit Boundary-Layer State in Subsonic Turbulent Jets," *Journal of Fluid Mechanics*, Vol. 851, 2018, pp. 83–124. doi:10.1017/jfm.2018.476.

[26] Huber, J., and Illa, S., "Jet Noise Assessment and Sensitivity at Aircraft Level," *28th AIAA Aeroacoustics Conference*, AIAA Paper No. 2007-3728, Reston, Virigina, 2007. doi:10.2514/6.2007-3728.

[27] Rumpfkeil, M., and Zingg, D., "Unsteady Optimization Using a Discrete Adjoint Approach Applied to Aeroacoustic Shape Design," *46th AIAA Aerospace Sciences Meeting and Exhibit*, AIAA Paper No. 2008-18, Reston, Virigina, 2008, pp. 1–9. doi:10.2514/6.2008-18.

[28] Freund, J. B., "Adjoint-Based Optimization for Understanding and Suppressing Jet Noise," *Journal of Sound and Vibration*, Vol. 330, No. 17, 2011, pp. 4114–4122. doi:10.1016/j.jsv.2011.02.009.

[29] Kim, J., Bodony, D. J., and Freund, J. B., "Adjoint-Based Control of Loud Events in a Turbulent Jet," *Journal of Fluid Mechanics*, Vol. 741, 2014, pp. 28–59. doi:10.1017/jfm.2013.654.

[30] Patel, T. K., and Miller, S. A. E., "Statistical Sources for Broadband Shock-Associated Noise using the Navier-Stokes Equations," *The Journal of the Acoustical Society of America*, 2020. (Accepted - To Appear) Accepted : 11th November 2019.

[31] Miller, S. A. E., "Noise from Isotropic Turbulence," *AIAA Journal*, Vol. 55, No. 3, 2017, pp. 755–773. doi:10.2514/1.J055114.

[32] Tam, C. K. W., and Auriault, L., "Mean Flow Refraction Effects on Sound Radiated from Localized Sources in a Jet," *Journal of Fluid Mechanics*, Vol. 370, 1998, pp. 149–174. doi:10.1017/S0022112098001852.

[33] Miller, S. A. E., and Morris, P. J., "The Prediction of Broadband Shock-Associated Noise Including Propagation Effects," *International Journal of Aeroacoustics*, Vol. 11, No. 7-8, 2012, pp. 755–781. doi:10.1260/1475-472X.11.7-8.755.

[34] Henry, C., Bailly, C., and Bodard, G., "Stochastic Prediction of Broadband Shock-Associated Noise Including Propagation Effects." *Proceedings of the Acoustics 2012 Nantes Conference*, Nantes, France, 2012, pp. 2341–2346.

[35] Blackstock, D. T., *Fundamentals of Physical Acoustics*, John Wiley & Sons, 2000.

[36] Tam, C. K. W., and Auriault, L., "Jet Mixing Noise from Fine-Scale Turbulence," *AIAA Journal*, Vol. 37, No. 2, 1999, pp. 145–153. doi:10.2514/2.691.

[37] Lighthill, M. J., "On Sound Generated Aerodynamically I. General Theory," *Proceedings of the Royal Society of London. Series A. Mathematical, Physical and Engineering Sciences*, Vol. 211, No. 1107, 1952, pp. 564–587. doi:10.1098/rspa.1952.0060.

[38] Ribner, H. S., "Theory of Two-Point Correlations of Jet Noise," *NASA TN D-8330*, 1976.

[39] Menter, F. R., "Two-Equation Eddy-Viscosity Turbulence Models for Engineering Applications," *AIAA Journal*, Vol. 32, No. 8, 1994, pp. 1598–1605. doi:10.2514/3.12149.

[40] Biedron, R. T., Carlson, J.-R., Derlaga, J. M., Gnoffo, P. A., Hammond, D. P., Jones, W. T., Kleb, B., Lee-Rausch, E. M., Nielsen, E. J., Park, M. A., Rumsey, C. L., Thomas, J. L., Thompson, K. B., and Wood, W. A., "FUN3D Manual 13.4," *NASA/TM-2018-220096*, 2018.

[41] Pope, S. B., *Turbulent Flows*, Cambridge University Press, Cambridge, U.K., 2000.

[42] Kolmogorov, A. N., "The Local Structure of Turbulence in Incompressible Viscous Fluid for Very Large Reynolds Numbers," *Proceedings of the Royal Society A: Mathematical, Physical and Engineering Sciences*, Vol. 434, No. 1890, 1991, pp. 9–13. doi:10.1098/rspa.1991.0075.

[43] Ishihara, T., Yoshida, K., and Kaneda, Y., "Anisotropic Velocity Correlation Spectrum at Small Scales in a Homogeneous Turbulent Shear Flow," *Physical Review Letters*, Vol. 88, No. 15, 2002, p. 154501. doi:10.1103/PhysRevLett.88.154501.

[44] Brown, C., and Bridges, J. E., "Small Hot Jet Acoustic Rig Validation," *NASA/TM-2006-214234*, 2006.

[45] Rice, T., "2D and 3D Method of Characteristic Tools for Complex Nozzle Development Final Report," *NASA/RTDC-TPS-481*, 2003.

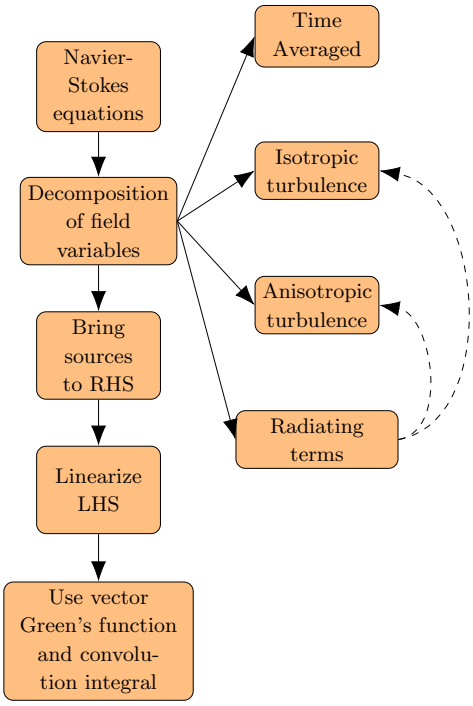

Fig. 1 Flowchart of the acoustic analogy based on the decomposition of the Navier-Stokes equations.

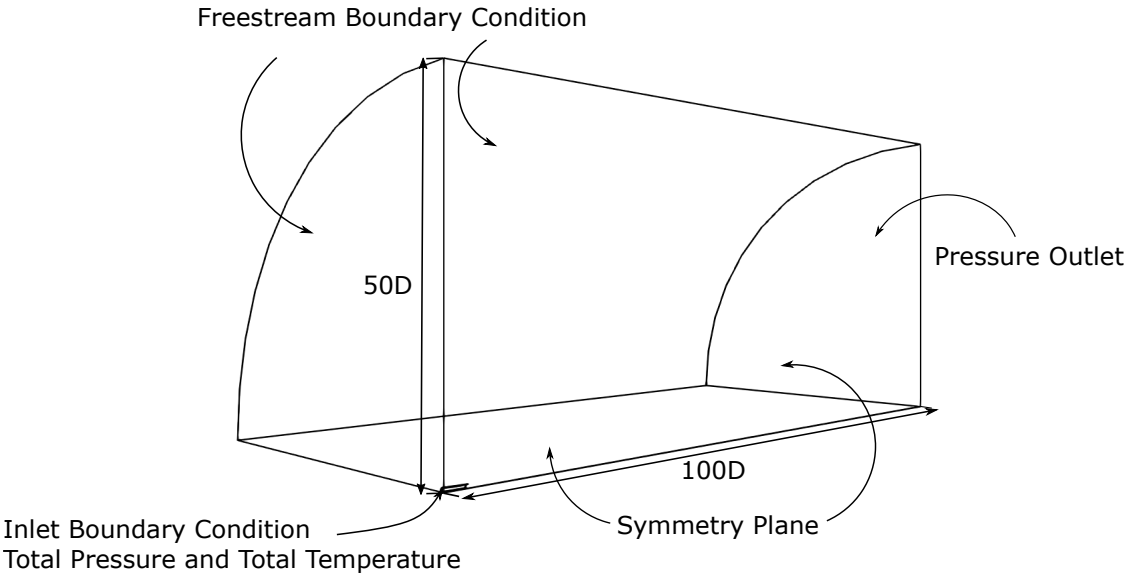

Fig. 2 The computational domain with specified boundary conditions.

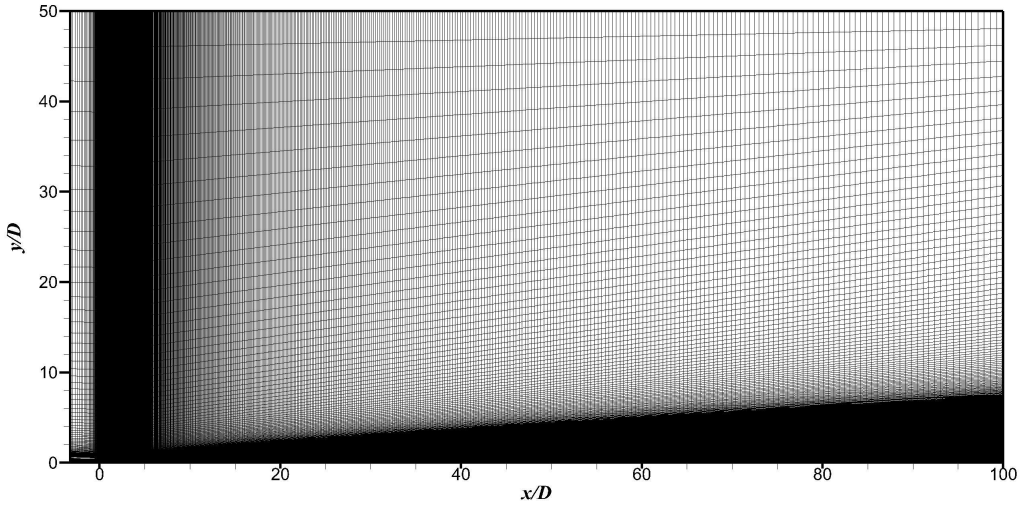

(a)

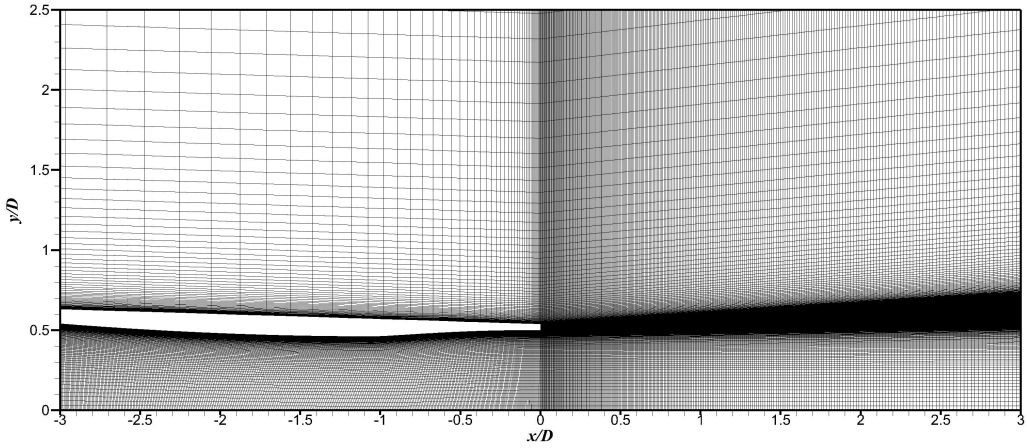

(b)

Fig. 3 Computational mesh shown for (a) entire domain and (b) near nozzle region.

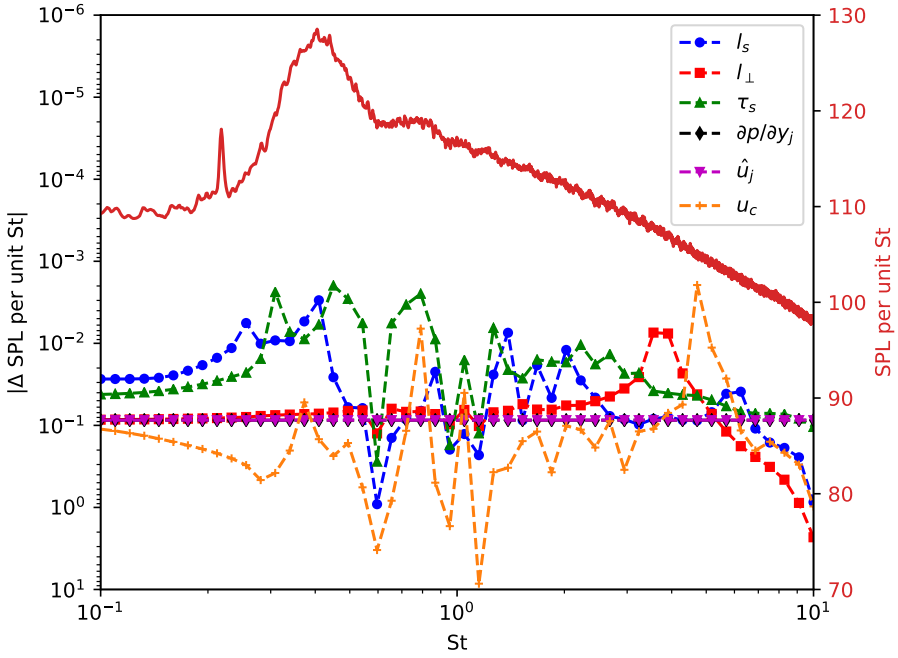

Fig. 4 Sensitivity of various model parameters. The red solid line represents the experimental spectrum. The dashed lines with different symbols represent the sensitivity of various parameters in the model.

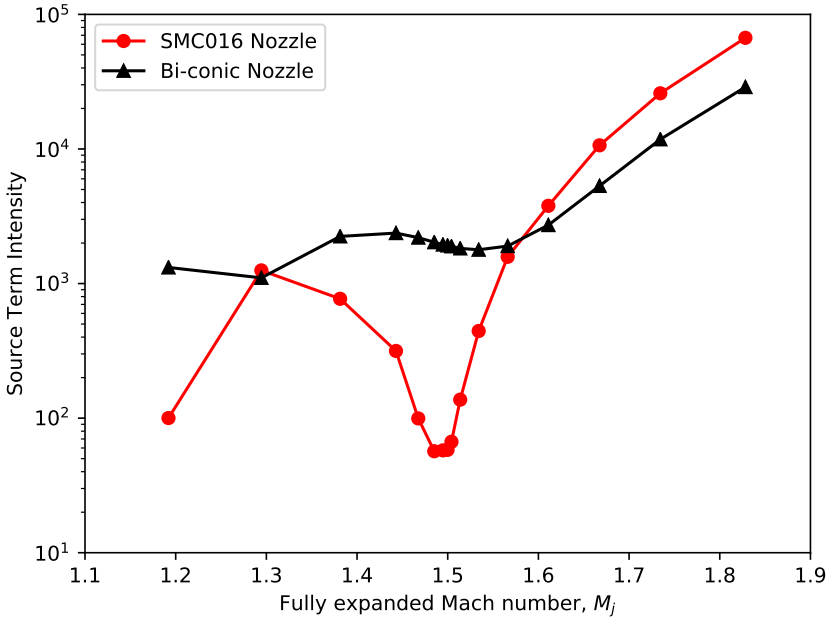

Fig. 5 Comparison of BBSAN intensity for SMC016 nozzle and biconic nozzle at different NPR.

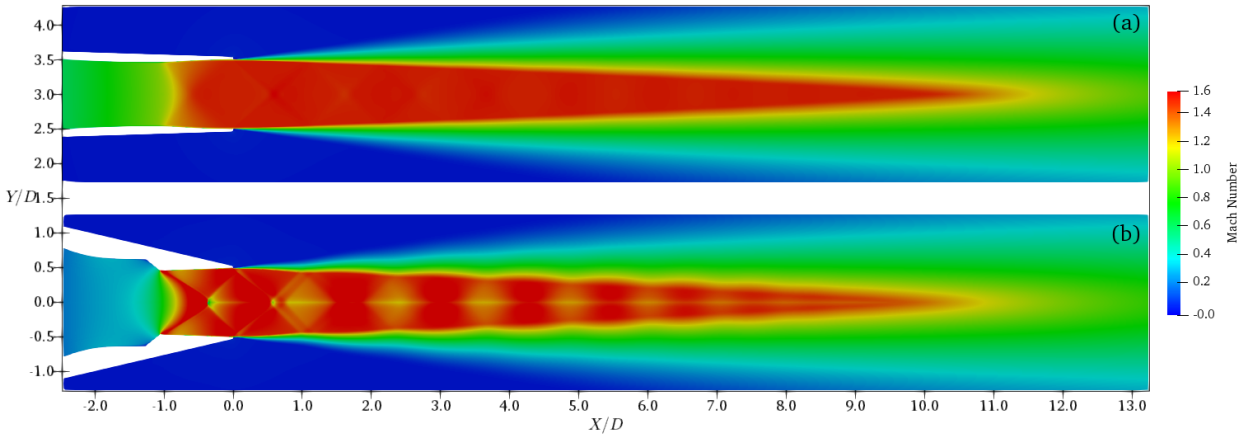

Fig. 6 Mach number contours of (a) SMC016 nozzle and (b) biconic nozzle operating at design condition.

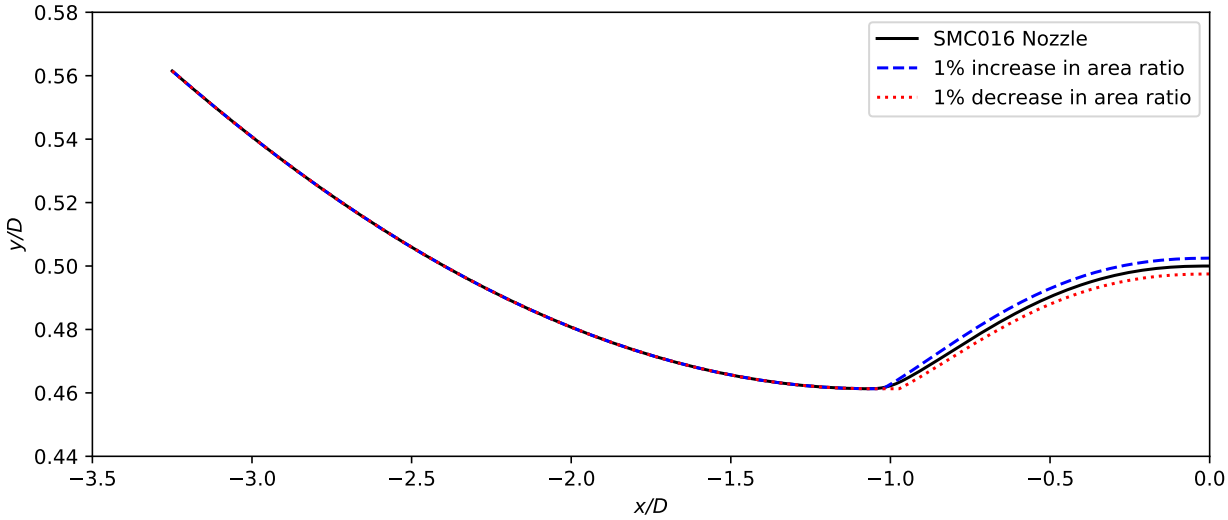

Fig. 7 Perturbed nozzle contours designed using MOC.

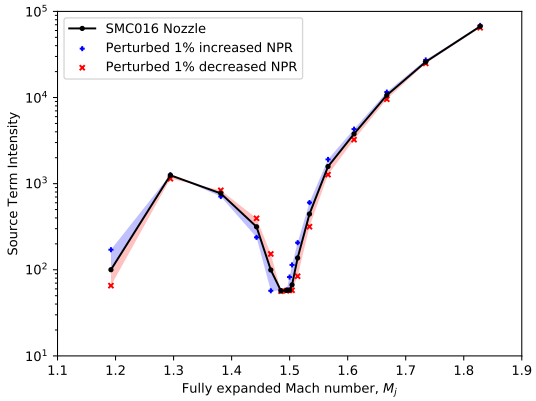

(a) Sensitivity of the source term intensity with perturbed NPR.

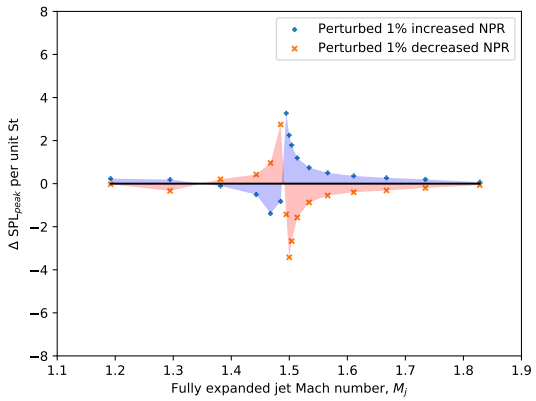

(b) Variation in SPL per unit St with perturbed NPR.

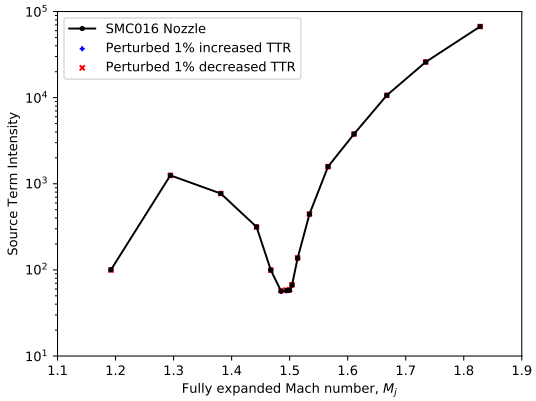

(c) Sensitivity of the source term intensity with perturbed TTR.

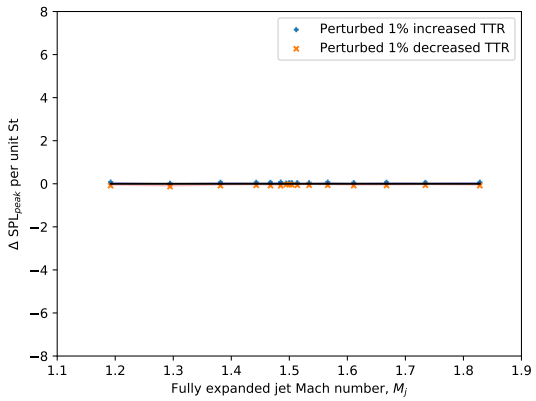

(d) Variation in SPL per unit St with perturbed TTR.

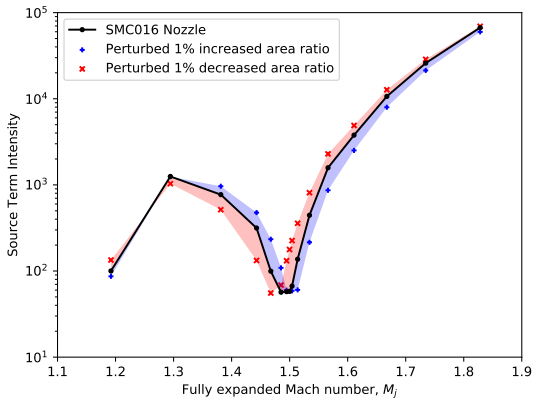

(e) Sensitivity of the source term intensity with perturbed area ratio.

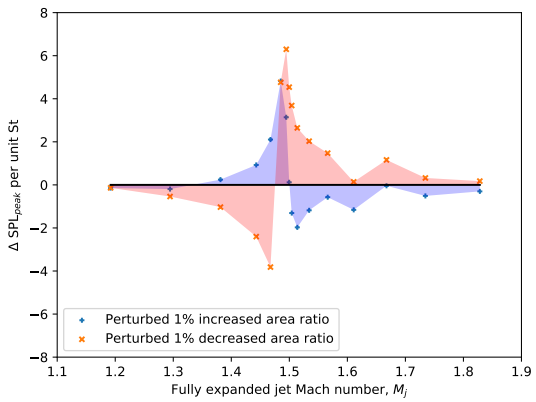

(f) Variation in SPL per unit St with perturbed area ratio.

Fig. 8 Sensitivity studies for an SMC016 nozzle.

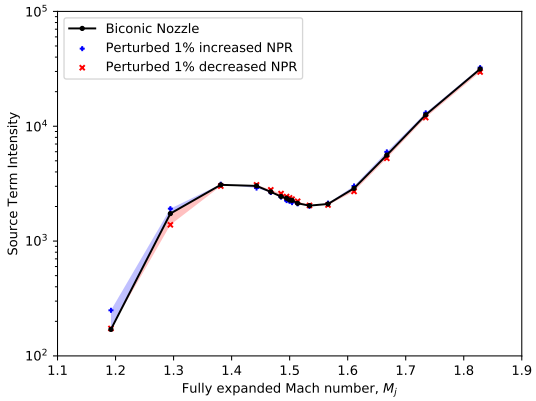

(a) Sensitivity of the source term intensity with perturbed NPR.

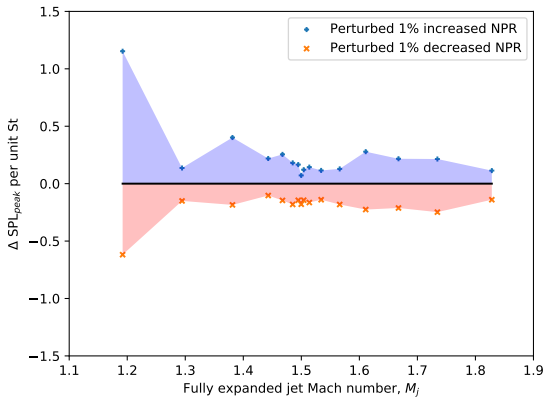

(b) Variation in SPL per unit St with perturbed NPR.

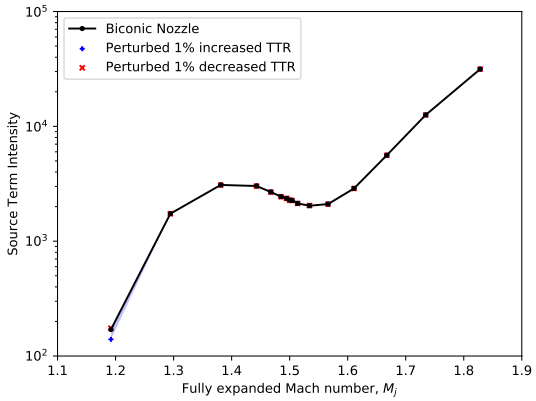

(c) Sensitivity of the source term intensity with perturbed TTR.

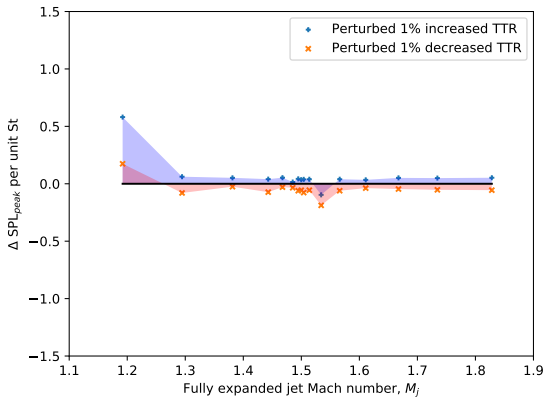

(d) Variation in SPL per unit St with perturbed TTR.

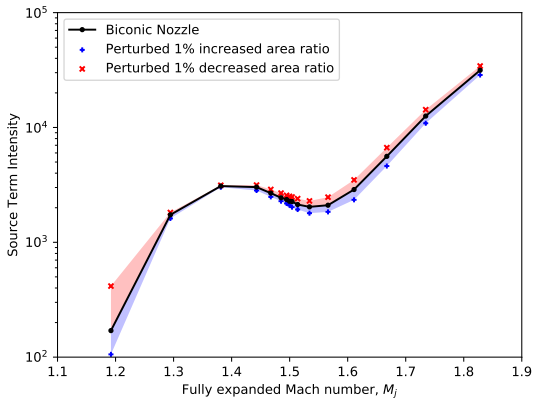

(e) Sensitivity of the source term intensity with perturbed area ratio.

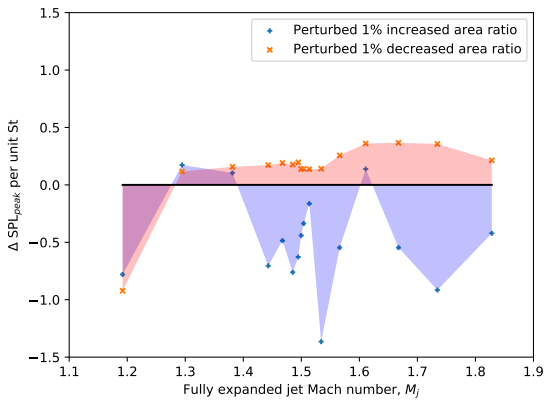

(f) Variation in SPL per unit St with perturbed area ratio.

Fig. 9 Sensitivity studies for a biconic nozzle.

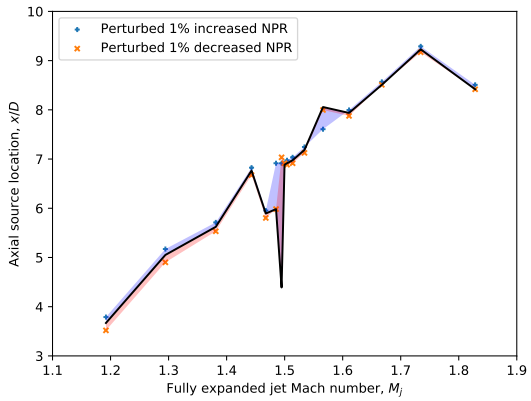

(a) Axial source location for SMC016 nozzle with perturbed NPR.

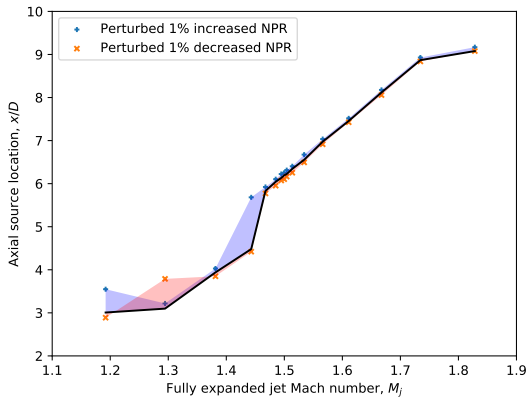

(b) Axial source location for biconic nozzle with perturbed NPR.

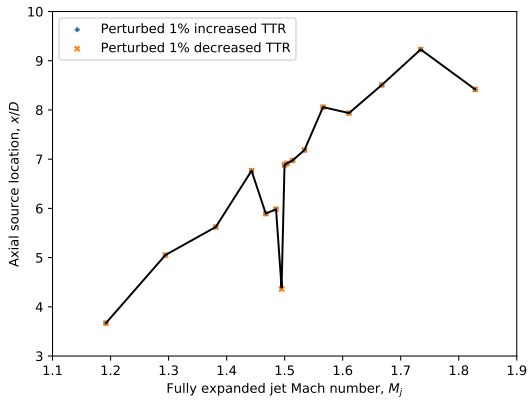

(c) Axial source location for SMC016 nozzle with perturbed TTR.

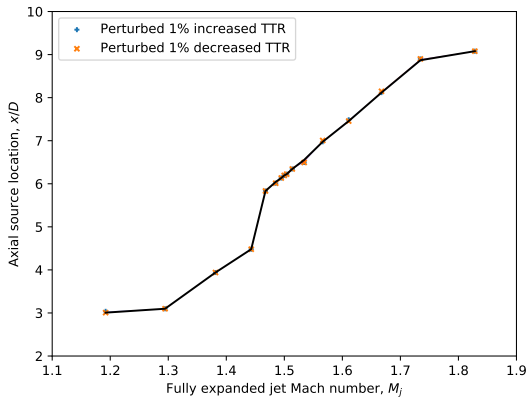

(d) Axial source location for biconic nozzle with perturbed TTR.

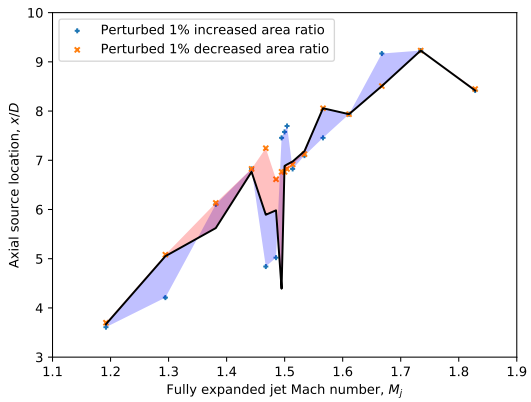

(e) Axial source location for SMC016 nozzle with perturbed area ratio.

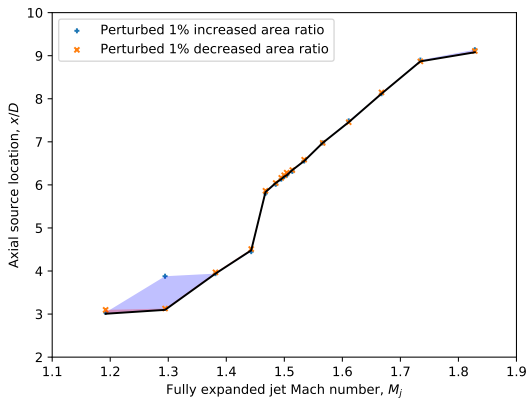

(f) Axial source location for biconic nozzle with perturbed area ratio.

Fig. 10 Sensitivity studies for axial source location.

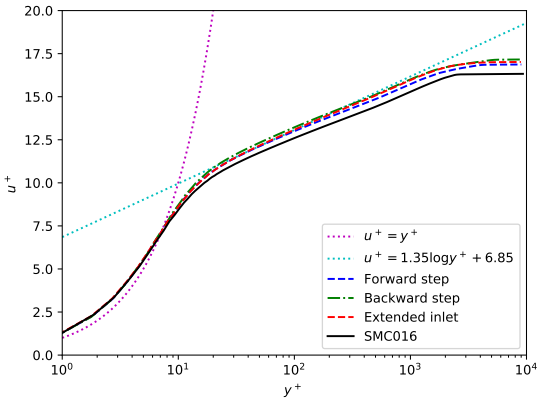

(a) Boundary layer profile plotted using the inner coordinates. The dotted lines (...) represent the viscous sublayer and the log layer regions.

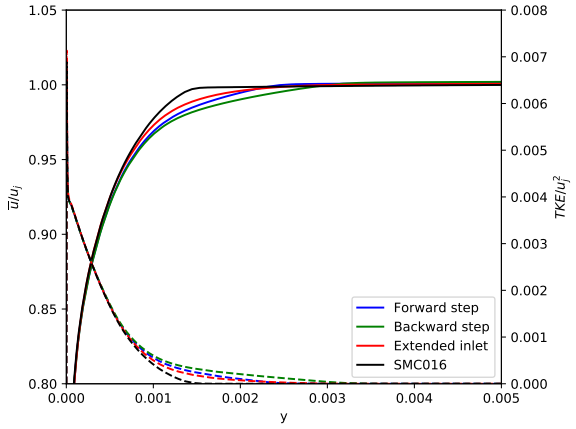

(b) Boundary layer profile plotted using the outer coordinates. The solid lines (–) represent the mean axial velocity and the dashed lines (- -) represent the turbulent kinetic energy.

Fig. 11 Boundary layer profile at the exit of the nozzle.

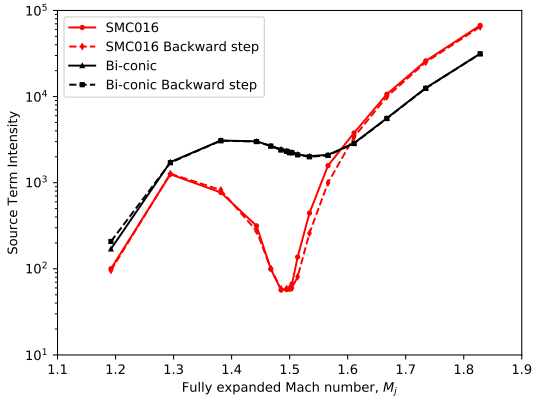

(a) Source term intensity.

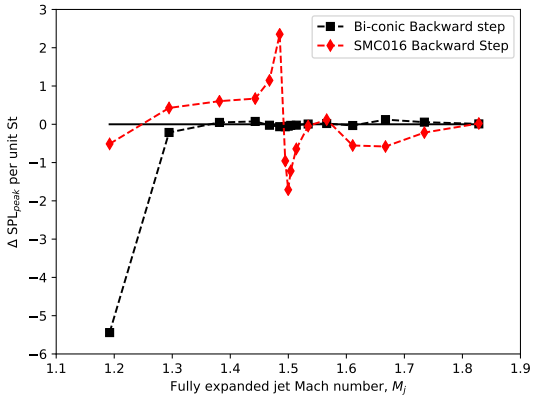

(b) Change in SPL per unit St.

Fig. 12 Sensitivity studies due to change in the boundary layer.